

Remixing Functionally Graded Structures: Data-Driven Topology Optimization with Multiclass Shape Blending

Yu-Chin Chan¹, Daicong Da¹, Liwei Wang^{1,2} and Wei Chen^{1*}

^{1*}Dept. of Mechanical Engineering, Northwestern University,
Evanston, 60208, IL, USA.

²State Key Laboratory of Mechanical System and Vibration,
School of Mechanical Engineering, Shanghai Jiao Tong
University, Shanghai, China.

*Corresponding author(s). E-mail(s): weichen@northwestern.edu;
Contributing authors: ychan@u.northwestern.edu;
dda@northwestern.edu; iridescence@sjtu.edu.cn;

Abstract

To create heterogeneous, multiscale structures with unprecedented functionalities, recent topology optimization approaches design either fully aperiodic systems or functionally graded structures, which compete in terms of design freedom and efficiency. We propose to inherit the advantages of both through a data-driven framework for multiclass functionally graded structures that mixes several families, i.e., classes, of microstructure topologies to create spatially-varying designs with guaranteed feasibility. The key is a new multiclass shape blending scheme that generates smoothly graded microstructures without requiring compatible classes or connectivity and feasibility constraints. Moreover, it transforms the microscale problem into an efficient, low-dimensional one without confining the design to predefined shapes. Compliance and shape matching examples using common truss geometries and diversity-based freeform topologies demonstrate the versatility of our framework, while studies on the effect of the number and diversity of classes illustrate the effectiveness. The generality of the proposed methods supports future extensions beyond the linear applications presented.

Keywords: Topology optimization, Functionally graded structure, Multiscale, Multiclass, Shape interpolation, Data-driven design

1 Introduction

Multiscale mechanical structures present exciting functionalities and unprecedented performance ranging from global objectives like light-weighting, thermal conductivity and energy absorption (Wu et al, 2021; Da et al, 2019; Jia et al, 2021; Da et al, 2021) to targeted local behaviors such as shape morphing or pattern reconfiguration for soft robots (Mirzaali et al, 2018; Boley et al, 2019) and active airfoils (Lumpe and Shea, 2021). To design such complex structures, multiscale topology optimization (TO) has risen to prominence and flourished. While early research focused on periodic microstructures (also known as unit cells or building blocks), two types of *heterogenous* designs, in which neighboring microstructural topologies differ from each other, now surpass them in terms of performance: fully aperiodic systems (Schumacher et al, 2015; Panetta et al, 2015; Zhu et al, 2017) and functionally graded structures (FGS) (Panesar et al, 2018). In this work, we aim to bridge the freedom of aperiodic designs with the efficiency and smooth interfaces of FGS.

Although aperiodic structures allow immense design freedom – a different microstructure at every location – they come at the cost of explosive problem sizes. Two avenues of data-driven methods have emerged to counter this ”curse of dimensionality”. One assembles microstructures from pre-computed libraries via combinatorial optimization (Schumacher et al, 2015; Panetta et al, 2015; Coulais et al, 2016; Ferrer et al, 2018), and the other accelerates gradient-based design by creating deep learning (DL) models from massive datasets for dimension reduction and rapid property predictions (Wang et al, 2020a; Kumar et al, 2020).

These approaches are powerful, but require large overhead costs to build the datasets and models, and need careful strategies to select reasonably compatible neighboring microstructures. Even then, they may not achieve connectivity on par with FGS. Combined with the use of the effective, homogenized properties, low connectivity can result in the manufactured performance deviating greatly from the optimized design. These drawbacks mean that, in their current state, data-driven methods are difficult to scale to large systems with heterogeneity and complex physics, e.g., nonlinear mechanics. Compared to FGS, such approaches are less suitable when stress concentrations or expensive property simulations must be avoided.

In contrast, the continuous interfaces of FGS can mitigate the errors from homogenization as well as the discrepancies between the intended and manufactured designs (Garner et al, 2019; Panesar et al, 2018). Functional grading can be further categorized into three camps: spatially-varying volume fraction (Wang et al, 2018; Li et al, 2019; Zong et al, 2019; Jansen and Pierard, 2020), topology (Kumar et al, 2020; Sanders et al, 2021), or a hybrid of both (Wang et al, 2020c; Luo et al, 2021). While traditional FGS use the first, recent research is shifting towards the latter two, which have demonstrated that expanding the design space to include multiple topology types can considerably improve the structural performance. Our work belongs to the hybrid one, and to facilitate ease of discussion, we define a *microstructure class* as

a family of microstructures that possess the same overall topological concept but vary individually by volume fraction. Hence, the works in the last two categories can be termed *multiclass*.

Within existing multiclass methods, the prevailing strategy is to treat FGS design as a multi-material TO problem by allocating each class to its own region with distinct boundaries. This assumes that the interfaces between classes are perfectly connected. As a result, most approaches pre-define a few mutually compatible classes (Wang et al, 2020c; Luo et al, 2021) or fix their connections (Deng et al, 2019; Chu et al, 2019; Zhang et al, 2018), which reduces computational cost and complexity but can yield suboptimal solutions.

Similar methods in the general multiscale TO field accomplish connected heterogeneous designs without the above simplifications by: (1) sharing finite elements and design variables at interfaces (Liu et al, 2019), (2) adding connectivity constraints (Du et al, 2018; Garner et al, 2019), (3) controlling the change in the properties of intermediate microstructures (Zhou et al, 2019), (4) creating geometric gradations during pre- or post-processing (Sanders et al, 2021; Zhou et al, 2019; Zobaer and Sutradhar, 2020), and (5) interpolating random field representations of microstructures (Kumar et al, 2020). Of these, Liu et al (2019), Garner et al (2019), and Sanders et al (2021) concurrently design the macrostructure as well as the distributions of multiple microstructures, and only Luo et al (2021) also optimized the graded volume fractions. Moreover, many do not scale well with the number of classes.

Merging the advantages of the two heterogeneous approaches, we propose a general TO framework for multiclass FGS that achieves smooth transitions between multiple microstructure classes without additional constraints, even if those classes are not compatible initially. The cornerstone of our approach is a novel multiclass shape blending scheme that generates new microstructures from a small set of predefined basis classes while guaranteeing certain aspects of feasibility. Our framework departs from existing heterogeneous design methods in several ways:

- First, we create a continuous and low-dimensional microstructure representation by using the parameters of our shape blending scheme as design variables. This transforms the microscale problem into a parametric one without using costly, geometry-based DL. While we do require predefined basis classes, this by no means restricts our design, as we allow the regions for each class and the boundaries between them to be blurred so that the microstructures anywhere in the FGS can be novel, i.e., not found in the initial basis classes.
- Second, our blending scheme integrates naturally into existing TO methods. In this work, we incorporate it with discrete and gradient-based TO, along with a new penalty that promotes diverse designs. These significantly reduce the cost to concurrently optimize the macrostructure as well as the graded topologies, volume fractions, and distributions of any number of microscale classes. Thus, through blending, our framework features design

freedom near that of aperiodic methods while inheriting the efficiency of functionally graded design.

- Moreover, the blending parameters serve as effective inputs for feedforward neural networks that predict the effective properties of new microstructures and can be re-used in multiple applications, further accelerating design.
- Finally, the blending scheme can build in certain feasibility metrics (e.g., self-connectedness and minimum feature size) so that they do not need to be included explicitly in the TO problem. Furthermore, the flexibility of using basis classes permits designers to incorporate expert knowledge and eliminates the frustration of choosing compatible classes. If desired, manual selection can be removed altogether by extracting classes from open-source databases, e.g., using diversity metrics (Chan et al, 2020).

With compliance and shape morphing examples, we demonstrate the efficiency and inherent ability of our approach in designing multiscale structures with continuous transitions. The benefits of multiclass FGS are verified by utilizing both common truss-type and diverse freeform (topology-optimized) basis classes, and by comparing our results to designs in literature.

2 Methodology

In this section, we introduce three crucial components in our approach: (1) multiclass shape blending and global interpolation schemes (Sec. 2.1), (2) neural networks for property prediction (Sec. 2.2), and (3) concurrent multiclass data-driven topology optimization (TO), which ties all of the methods into one framework (Sec. 2.3).

2.1 Multiclass Shape Blending and Smooth Interpolation

2.1.1 Background

Our proposed shape blending scheme is heavily inspired by the computer graphics field, where morphing one geometric model into another has long been studied and utilized in, e.g., animation films and video games (Sanchez et al, 2015; Rohra and Kulkarni, 2019). These methods have also supported applications like medical imaging (Carballido-Gamio et al, 2005) and metal-forming manufacturing simulations (Thomas et al, 2020). In fact, evolving geometries through surface representations (Breen and Whitaker, 2001) and partial differential equations (Bojsen-Hansen et al, 2012) is the foundation of the popular level-set TO method, while combining shapes using distance fields is the bedrock of TO algorithms that use geometry projection (Smith and Norato, 2020) and Movable Morphing Components (Zhang et al, 2015).

Most closely related to the interest of this paper are blending techniques that use function representations (FReps) of shapes, which parametrize any geometric model as a series of operations (e.g., unions, differences, and intersections) performed on a set of primitives or basis geometries (Sanchez, 2016).

It is extremely flexible as it allows the bases to be defined by any representation, e.g., meshes or voxels, and any resolution. In our case, we represent our basis microstructure classes as continuous signed distance fields (SDFs), which are implicit function representations similar to level-sets. That is, the sign of the field determines whether the material is solid or void at any arbitrary point (x, y) within the microstructure domain, D , as follows:

$$\begin{cases} \Phi(x, y, t) > 0 & (x, y) \in \Omega \\ \Phi(x, y, t) = 0 & (x, y) \in \Gamma \\ \Phi(x, y, t) < 0 & (x, y) \in D/\Omega \end{cases}, \quad (1)$$

where Φ is the SDF, Ω is the solid region, and Γ is the boundary of the solid structure. The isovalue t controls the isocontour of the field and therefore enables us to tune volume fractions. With this powerful representation, we can not only generate an entire family of microstructures over a continuous range of volume fractions, but also combine multiple SDFs to create novel classes.

Blending operations to mix SDFs have been studied for decades, beginning with the simple set-theoretic operation for the union of the function representations of two shapes, Φ_1 and Φ_2 (Ricci, 1973):

$$\Phi_{union} = \max(\Phi_1, \Phi_2). \quad (2)$$

Since then, many works have improved metamorphosis using function-based operations (Sanchez, 2016; Shapiro, 2007), optimization (Eisenberger et al, 2019), and DL-based interpolation (Oring et al, 2020; Gu et al, 2019). However, these can require intensive user-interaction and computational costs, and are, therefore, intractable or unsuitable for multiscale design.

2.1.2 Multiclass Shape Blending Scheme

Rather than using complex formulations, our proposed multiclass shape blending scheme is a combination of two simple techniques: (1) a weighted sum of basis classes based on cross dissolving, and (2) an activated union with the lower feasible bounds of each basis. The entire scheme is differentiable and efficient, which fits in well with gradient-based optimization algorithms.

Crucial to our scheme are basis microstructure classes, which do not need to be mutually compatible. We denote the SDF representations of arbitrary basis classes as Φ_d^B for $d = 1, \dots, D$, where the shapes Φ_d^B and total number of classes D can be defined by the user. Note that while we use truss-type bases in this section’s figures as demonstration, our method is applicable to any set of classes.

Prior to blending, we normalize the D basis classes so that they can be mixed fairly, and also find their lower feasible bounds. The following pre-processing steps only need to be performed once per set of bases:

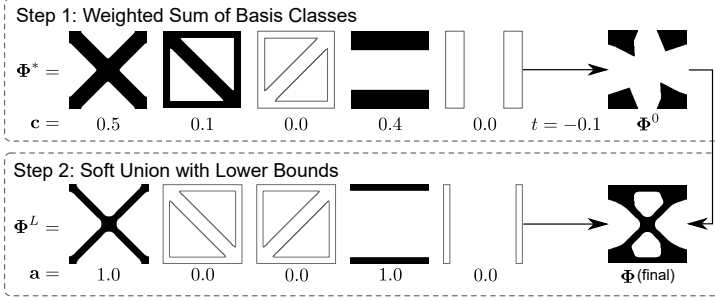


Fig. 1: Illustration of using multiclass shape blending scheme to generate a microstructure from truss basis classes. Outlined shapes represent classes whose weights are zero. Step 1 (top row; Eq. 3) may cause broken shapes, but Step 2 (bottom row; Eq. 4) ensures the final microstructure, Φ , is feasible.

1. Choose a common volume fraction, v^* , and find the representative SDF for each basis, $\Phi_d^* = \Phi_d^B + t_d^*$, such that it has v^* . We use the well-known bisection algorithm.
2. Find the SDF of the lower feasible bound of each basis, $\Phi_d^L = \Phi_d^B + t_d^L$, using any desired feasibility metric. In this work, we set a minimum feature size of 4 pixels for a 50×50 microstructure.

After this one-time process, we can use Φ_d^* and Φ_d^L repeatedly for our proposed multiclass blending. The first step of the scheme is based on cross dissolving (Rohra and Kulkarni, 2019), which can be simply defined as a linear interpolation between the source and target geometries. This can induce a double exposure effect where traces of both shapes co-exist in the blended result. While that causes unnatural morphing of, e.g., human faces, it organically achieves connected transitions between neighboring microstructures.

We express multiclass interpolation as a weighted sum of the bases:

$$\Phi^0 = \sum_d^D c_d \Phi_d^* + t, \quad (3)$$

where $c_d \in [0, 1]$. Although it effectively creates new classes of microstructures, this interpolation is agnostic to important geometrical features and can lead to broken shapes that have disconnected or thin features (see the top row of Fig. 1).

Therefore, to guarantee that the blended microstructures are sufficiently connected and feasible, we propose an additional step that enforces a lower feasible bound on blending. It also acts as an implicit constraint for simple manufacturing considerations, e.g., minimum feature sizes or volume fractions. This second step is an activated soft-max function, a continuous and

differentiable extension of the set-theoretic union above (Eq. 2):

$$\Phi = \frac{1}{\beta_2} \log \left[\exp(\beta_2 \Phi^0) + \sum_d^D a_d \exp(\beta_2 \Phi_d^L) \right], \quad (4)$$

where a_d are the activated weight parameters using the Heaviside function:

$$a_d = H(c_d, \beta_2, \eta_2) = \frac{\tanh(\beta_2 \eta_2) + \tanh(\beta_2 (c_d - \eta_2))}{\tanh(\beta_2 \eta_2) + \tanh(\beta_2 (1 - \eta_2))}. \quad (5)$$

By setting the threshold $\eta_2 > 0$, the activation guarantees that the minimum feasible bound of at least one – but not all, or else low volume fractions would be difficult to attain – of the bases are present in each blended result. That is, in this step, only weights that are greater than η_2 are activated to equal one (shaded shapes in the second panel of Fig. 1) while others are suppressed to zero (outlined shapes in Fig. 1). We find that setting η_2 to the 75th-percentile of the weights, \mathbf{c} , works quite well in promoting connected transitions.

With the two-step shape blending scheme, the representation of all possible blended microstructures, including those in the original basis classes, can be compactly expressed as the weight parameters. We can, therefore, formulate the microscale design variables as $\mathbf{c}^{(m)}$ for $m = 1, \dots, M$ desired optimal classes, transforming the typically high-dimensional optimization problem into a simple and efficient parametric one that can still generate a wide range of microstructures.

A final note regarding microstructure design is that, in practice, Eq. 3 allows each $c_d^{(m)} \in [0, 1]$ and can lead to $\sum_{d=1}^D c_d^{(m)} = 0$, which results in completely solid microstructures and occasional numerical issues. Moreover, it causes redundancy in the design space since taking $\Phi^0 \geq 0$ to obtain the solid topology cancels out the least common denominator of the weights. There are numerous ways to enforce the sum of $c_d^{(m)}$ to be equal to one, such as multi-material interpolation schemes in TO. We extend one such scheme from our previous work (Chan et al, 2019) to normalize the basis class weights as follows:

$$\tilde{\mathbf{c}}^{(m)} = \mathbf{z}^{(1)} + \sum_{j=1}^{D-1} \left[(\mathbf{z}^{(j+1)} - \mathbf{z}^{(j)}) \prod_{k=1}^j c_k^{(m)} \right], \quad (6)$$

where $\mathbf{z}^{(j)}$ are constant one-hot encoded vectors for each basis such that $z_i^{(j)}$ equals 1 for $i = j$ and 0 for all $i \neq j$. Subsequently, c_d in Eqs. 3 and 5 are replaced with \tilde{c}_d . While our shape blending and design methods work well without Eq. 6, for increased stability in the optimization process, and the added bonus of reducing the microscale design variables, $\mathbf{c}^{(m)}$, to size $[1 \times D - 1]$, we use it in the remaining discussions.

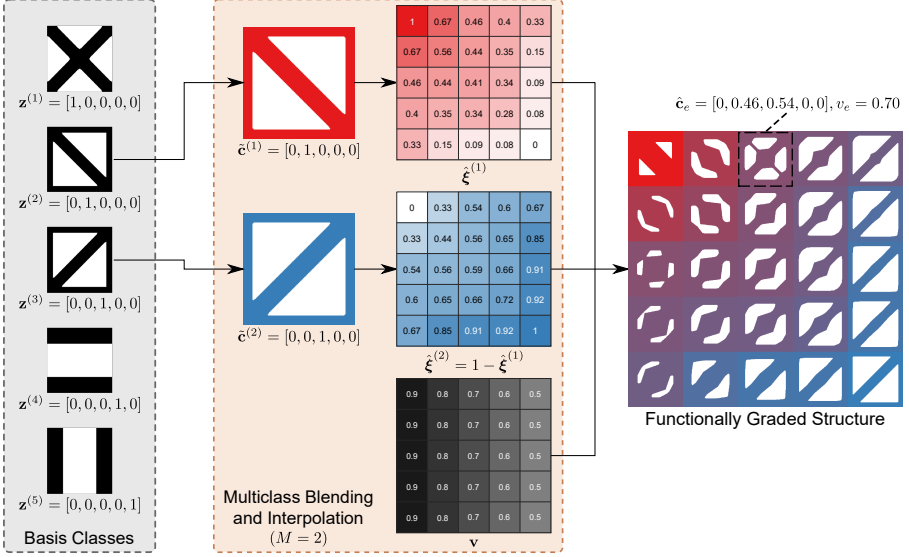


Fig. 2: Demonstration of the integration of multiclass shape blending and global interpolation. The basis classes are defined (left). Examples of $M = 2$ new classes, $\tilde{\mathbf{c}}^{(m)}$, their distributions, $\hat{\boldsymbol{\xi}}^{(m)}$, and volume fractions, \mathbf{v} , are given (middle). Each microstructure in the FGS (right) is generated by using Eq. 8.

2.1.3 Integration with Multiscale Design

In the context of multiscale design, the subscript e is added to denote individual microstructures, which each resides in one macroscopic quadrilateral 4-node finite element. Instead of directly optimizing the weights of each microstructure, we reduce the number of design variables by optimizing M new classes and interpolating them throughout the global structure using the distribution fields $\hat{\boldsymbol{\xi}}^{(m)}$. An example with $M = 2$ is portrayed by the red and blue classes in the middle panel of Fig. 2.

Similar to multi-material TO (and Eq. 6), we require that the sum of the distributions at each element equals one. Thus, to obtain each microstructure, e , we can globally interpolate the optimal class weights, $\tilde{\mathbf{c}}^{(m)}$, with:

$$\hat{\mathbf{c}}_e = \tilde{\mathbf{c}}^{(1)} + \sum_{j=1}^{M-1} \left[(\tilde{\mathbf{c}}^{(j+1)} - \tilde{\mathbf{c}}^{(j)}) \prod_{k=1}^j \hat{\xi}_e^{(k)} \right], \quad (7)$$

where $\hat{\xi}^{(m)}$ for $m = 1, \dots, M-1$ are the smoothed distribution fields after applying the radial filter found in TO methods (Sigmund, 2007) to encourage functional grading.

Therefore, combining Eqs. 3 through 7, our final multiclass shape blending scheme for a microstructure at element e is:

$$\Phi_e = \frac{1}{\beta_2} \log \left\{ \exp \left[\beta_2 \left(\sum_d^D \hat{c}_{e,d} \Phi_d^* + t_e \right) \right] + \sum_d^D a_{e,d} \exp \left(\beta_2 \Phi_d^L \right) \right\}, \quad (8)$$

where $a_{e,d} = H(\hat{c}_{e,d}, \beta_2, \eta_2)$ and t_e is found using the bisection algorithm to match a given or optimized volume fraction, v_e . This replaces Eq. 4 during optimization.

The process of blending and global interpolation to assemble a FGS is demonstrated in Fig. 2. For this, we use five truss-type basis classes and artificially create $M = 2$ new classes, $\tilde{\mathbf{c}}^{(m)}$, their distribution fields, $\hat{\xi}^{(m)}$, and volume fractions, \mathbf{v} . In practice, these parameters would be optimized. For each microstructure, e , in the FGS, its globally interpolated weights, $\hat{\mathbf{c}}_e$, are found via Eq. 7, and its SDF generated by the blending scheme in Eq. 8.

2.2 Property Prediction with Neural Networks

The continuous and low-dimensional microstructure representation lends itself well to one of the simplest deep learning (DL) techniques: regression with neural networks. More specifically, we can create feedforward neural networks with three or fewer hidden layers that predict the components of a microstructure’s effective stiffness tensor, \mathbf{C}_e^H , given the scalar values of the blending weights and volume fraction as inputs. That is, $\mathbf{C}_e^H = NN(\hat{\mathbf{c}}_e, \hat{v}_e)$, where $\hat{\mathbf{c}}_e$ and \hat{v}_e are the filtered (Sec. 2.3) class and volume fraction design variables, respectively.

After each hidden layer, we use a tanh activation function. For training, we use the mean squared error (MSE) loss and the Levenberg-Marquardt optimizer (Gavin, 2019). To include all possible microstructures, such as those where only a few basis classes have non-zero weights, we use an optimal sliced Latin hypercube method (Ba et al, 2015) to sample the weights c_d , first creating combinatorial ”slices”, then 20 space-filling samples for each ”slice”. To cover volume fractions, we also sample 15 microstructures from each resulting SDF (i.e., each set of weights) over $t \in [-1, 1]$. As an example, we obtain a total of 22,575 microstructures for $D = 5$ basis classes. The effective stiffness tensors of each are calculated using an energy-based homogenization method (Andreassen and Andreassen, 2014). We set aside 70%, 15%, 15% of the data for training, validation and testing.

Once the model is trained, we can use backpropagation (Hastie et al, 2009) to analytically derive the gradients of \mathbf{C}_e^H with respect to the design variables, $\hat{\mathbf{c}}_e$ and \hat{v}_e . This, together with the rapid predictions that bypass the cost of homogenization, allows the neural networks to significantly boost the efficiency of design.

2.3 Concurrent Multiclass Data-Driven Topology Optimization

One challenge in creating a concurrent functionally graded design framework that produces realistic results while remaining as general as possible is the different feasible ranges of arbitrary microstructure classes. Consider the five truss basis classes we used to demonstrate the blending scheme in Sec. 2.1. For a prescribed minimum feature size of 4 pixels, the first basis has a minimum feasible volume fraction of 0.2, while the second has a minimum of 0.4. The question that arises is: when different $v_{min} > 0$ are possible for each element e , how can we design the distribution of volume fractions while also optimizing a clearly defined macrostructure where some microstructures are allowed to be void (i.e., $v_e = 0$)?

Regarding this, most existing FGS research have either elected to ignore the macroscale design altogether (Li et al, 2019; Das and Sutradhar, 2020), or adopted a hybridized method that splits the macro- and micro-scale designs into two optimization problems (Wang et al, 2018; Jansen and Pierard, 2020; Chu et al, 2019; Zhang et al, 2018). None of these works incorporate multiclass designs where the basis topologies can be drastically different, however.

We propose to overcome this hurdle by merging parametric and non-parametric methods in a framework that utilizes evolutionary TO (BESO (Huang and Xie, 2007)) to optimize the discrete global structure, \mathbf{x} , and gradient-based TO solved by the method of moving asymptotes (MMA) (Svanberg, 1987) to design the classes, \mathbf{c} , their distributions, $\boldsymbol{\xi}$, and volume fractions, \mathbf{v} . The approach is similar to the latter group above, but unlike many, both scales are evolved simultaneously in one loop. This combination allows arbitrary sets of basis microstructures to be used rather than strict constraints or careful handpicking, and distinguishes our framework from others in terms of generality and efficiency.

Thus, the general optimization problem can be formulated as:

$$\begin{aligned}
 & \underset{\mathbf{c}, \mathbf{v}, \boldsymbol{\xi}, \mathbf{x}}{\text{minimize}} && f = f_{perf}(\mathbf{c}, \mathbf{v}, \boldsymbol{\xi}, \mathbf{x}) + k f_{div}(\mathbf{c}), \\
 & \text{subject to} && \mathbf{K}\mathbf{U} = \mathbf{F}, \\
 & && g_j \leq 0, \quad \forall j = 1, \dots, N_{con} \\
 & && 0 \leq c_d^{(m)} \leq 1, \quad \forall m = 1, \dots, M, \quad \forall d = 1, \dots, D-1, \\
 & && 0 \leq v_{min} \leq v_e \leq v_{max}, \quad \forall e = 1, \dots, N_{el}, \\
 & && 0 \leq \xi_e^{(m)} \leq 1, \quad \forall m = 1, \dots, M-1, \quad \forall e = 1, \dots, N_{el}, \\
 & && x_e \in \{x_{min}, 1\}, \quad \forall e = 1, \dots, N_{el},
 \end{aligned} \tag{9}$$

where f_{perf} is an application-dependent measure of design performance, f_{div} is a penalty on low class diversity (Sec. 2.3.1), N_{con} is the number of constraints g_j (if any), N_{el} is the number of macroscopic elements or microstructures, and M and D are the numbers of new (to be optimized) and basis classes, respectively. A small number such as $x_{min} = 1e-9$ is used to indicate void

microstructures to avoid numerical issues. The minimum volume fraction, v_{min} , is dependent on the chosen set of basis classes, i.e., $\min(\text{volume}(\Phi_d^L))$, whereas the upper bound, v_{max} , is 0.95.

We employ the traditional radial averaging filter (Sigmund, 2007) on our global-level design variables to avoid mesh dependency, resulting in the smoothed fields $\hat{\mathbf{v}}$, $\hat{\xi}^{(m)}$, and $\hat{\mathbf{x}}$. This additionally enforces the interface between optimal classes to be functionally graded, and that the macrostructure has a minimum feature size of r_{min} .

To update the designs, we use the default algorithms for BESO (Huang and Xie, 2007) and MMA (Svanberg, 1987). The only difference is that, to connect the two scales, the sensitivity number for BESO are dependent on the predicted effective properties of the microstructures. The derivations for this and all other sensitivities in our problem are shown in Appendix B.

In total, then, our multiclass FGS design framework has $(D-1)M + (M+1)N_{el}$ variables, where $M \leq D \ll N_{el}$. For the $M = 2$ MBB beam example (Fig. 4a), our method has 1,928 design variables. Perhaps the most comparable methods are the multilattice approach (Sanders et al, 2021), which needs 3,200 variables for the same problem without optimizing the graded volume fractions, and the latent variable multiclass approach (Wang et al, 2020c), which uses 1,920 variables and includes functionally graded volumes; both, however require predefined classes with fixed connectors. It is important to note that although it is possible for other methods to contain less design variables, they make simplifications that we do not.

2.3.1 Penalty to Encourage Convergence to Diverse Classes

Our method can enable high design freedom even with a low-dimensional microscale representation since blending allows the basis classes to mix continuously at both scales. Depending on the chosen optimizer, managing such complexity in two-scale design can be a challenge, one that is also encountered by existing multiscale methods. However, we propose that a cost-effective penalty on the objective function can aid the optimizer (in our case, MMA) without resorting to user-defined restrictions on the design space.

We introduce a penalty on low diversity between the M new classes, encouraging the microscale design variables, $\mathbf{c}^{(m)}$, to converge to values away from each other, so that the FGS is more likely to include different basis classes:

$$f_{div} = -\log [\det(L_{ij}(\mathbf{c}^{(i)}, \mathbf{c}^{(j)}))], \quad (10)$$

where $L_{ij} = \exp(-0.5 \|\mathbf{c}^{(i)} - \mathbf{c}^{(j)}\|_2^2)$ and $i, j \in 1, \dots, M$.

This is based on determinantal point processes (DPPs), which measure the diversity of a set of items (e.g., the classes $\mathbf{c}^{(m)}$ here) using a similarity matrix L_{ij} , where its elements are the similarities between the i -th and j -th pairs of data. The diversity can then be defined as the determinant of L_{ij} . A larger determinant value indicates that a set contains less similar items, spans a larger volume, and hence has greater diversity. More thorough coverage of

DPPs, as well as a deeper dive into the benefits of diversity for data-driven multiscale design, can be found in our previous work (Chan et al, 2020).

Intuitively, minimizing f_{div} is equivalent to maximizing the diversity of the new classes. Since the value of f_{div} approaches zero as classes become more diverse, i.e., the values of $c_d^{(i)}$ and $c_d^{(j)}$ grow farther apart, diversity serves as a natural penalty function. It needs only a weight k so that its value, typically within $[0, 1]$ after the first few iterations, can compete with the structural performance, f_{perf} . Moreover, it acts similarly to an L_2 regularizer that smooths the objective function as k increases, which may avoid sensitivity to initializations and help find an optimum faster in some non-convex or highly nonlinear problems. Indeed, we find in our case studies that adding the penalty help our optimizers to find more optimal solutions (Sec. 3.2).

2.3.2 Volume Relaxation and Adaptive Target Volume

If any volume constraints are defined in the design problem, we must have a way to obtain the continuous gradients of volume with respect to the parameters of the shape blending scheme. To achieve this, we can approximate the filtered volume fraction of a microstructure, \hat{v}_e , by transforming its SDF into a relaxed grayscale field, similar to that of density-based TO, using the Sigmoid function

$$S(\Phi, \beta_1) = \frac{1}{1 + \exp(-\beta_1 \Phi)}, \quad (11)$$

where β_1 is a fixed parameter to control the strength of relaxation. Thereafter, the approximate volume is

$$\hat{v}_e^a = \frac{1}{n_{el}} \sum_{u=1}^{n_{el}} S(\Phi_{e \cdot u}, \beta_1), \quad (12)$$

where n_{el} is the number of elements in the discretized SDF, and the sensitivity of $\partial V_{Global} / \partial \mathbf{c}_e$ is straightforward to calculate (see Appendix B).

In addition, low volumes are often a goal in multiscale design to take advantage of the porosity of the microstructures. By immediately applying a low volume fraction limit, however, it is possible to encounter infeasible and broken structures early in the optimization process (Christiansen et al, 2013; Andreasen et al, 2020). To avoid this, and to ensure that our macro- (BESO) and micro-scale (MMA) designs evolve at approximately the same rate, we use an adaptive scheme to lower the target volumes every 10 iterations. This is outlined in Algorithm 1, and the pseudo-code of the complete concurrent optimization framework is shown in Algorithm 2 of Appendix A.

3 Illustrative Examples

Through several problems in the linear elastic domain, we test the ability of our framework to achieve functional grading that is both smooth and feasible. Namely, we design two compliance and two target displacement, i.e., shape

morphing, examples. For each case, we study the effects of two sets of basis classes with different morphology types and initial mutual compatibility, as well as the number of new optimal classes, M . The basis classes and their associated DL models are shown in Sec. 3.1, the compliance studies in Sec. 3.2, and finally, the shape morphing examples in Sec. 3.3.

3.1 Basis Classes and Neural Networks

To illustrate the framework across a range of microstructure morphologies commonly found in literature, we use two sets of basis classes: one consisting of truss-type microstructures, and one of topology-optimized freeform shapes. Moreover, to show that human bias can be removed from the design without sacrificing much performance, we compare handpicking the truss basis to automatically selecting the freeform basis using diversity metrics.

3.1.1 Handpicked Simple Trusses

Some of the most popular microstructures in the TO field belong to truss-type classes, which possess both simple definitions and satisfactory performance (Panetta et al, 2015; Wang et al, 2020c; Luo et al, 2021; Chan et al, 2019). As such, they are fitting basis classes to validate the proposed framework. For our examples, we choose a set of bases that can, when combined in various ways, cover nearly all of the common truss morphologies in literature. Departing from other methods, we dial up the difficulty by defining the last two bases so that they are broken; to obtain feasible designs, these classes need to be either well-connected to their neighbors or blended with other bases that have self-connectedness. The five classes have already been shown several times in Figs. 1-2, as well as in Fig. 3a and b.

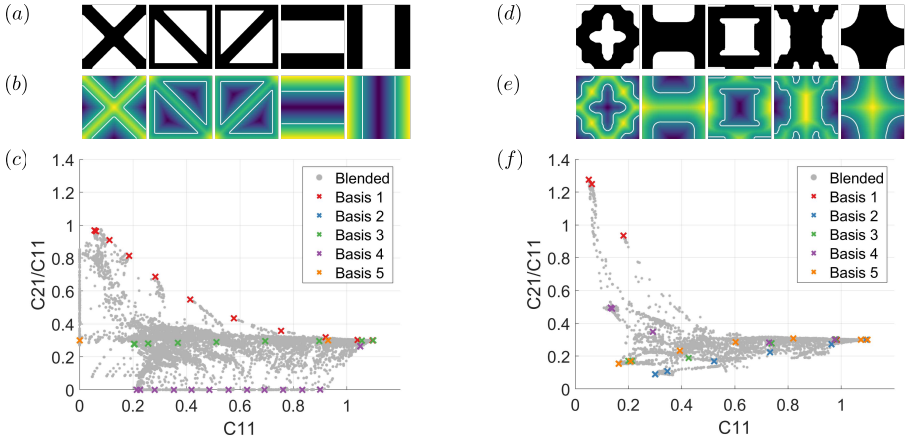


Fig. 3: (a) Truss basis classes represented as (b) SDFs (Φ_d^*), and (c) the property space of 22,575 blended microstructures by sampling $\{c, v\}$. (d) Freeform basis classes, (e) their SDFs, and (f) property space.

3.1.2 Shape and Property Diverse Freeform Subsets

We also assess the efficacy of our blending and interpolation schemes under even more challenging circumstances by defining a set of freeform basis classes with complex shapes derived from TO (Fig. 3d). They present interesting and highly illustrative case studies as their compatibility with each other is quite low. If used directly in design without our shape blending scheme, the feasibility of the final design would be extremely challenging to guarantee.

We collect these freeform classes from a different perspective, one where a designer has little prior knowledge and wishes to avoid using costly inverse optimization to find the basis microstructures. Thus, the five freeform classes are chosen by leveraging the open-source 2D metamaterials dataset (Wang et al, 2020b) and the automated diverse subset selection method (Chan et al, 2020) from our previous works. The method utilizes the DPPs introduced earlier (Sec. 2.3.1) to maximize the shape and property diversity of a subset of microstructures. By automatically covering a wide range of shapes and properties, we hypothesize that diverse basis classes can provide a high return on investment, attaining competent or even superior performance across multiple applications with less effort during the selection of bases.

We filter out any 50×50 microstructures with minimum feature sizes less than 4 pixels prior to applying our subset selection method. This eliminates some of the most complex shapes that provide little benefit for functional grading (e.g., microstructures with thin features that would limit the range of feasible volume fractions). To convert the selected binary microstructures into continuous SDF representations, we use the fast marching method (sk-, 2021). The shape and property diverse freeform basis classes shown in Fig. 3d and e.

3.1.3 Property Prediction Models

As discussed in Sec. 2.2, we obtain training datasets of 22,575 microstructures using sliced Latin hypercube sampling for each set of basis classes. The respective property spaces are depicted in Fig. 3c and f, where samples generated from blending are in gray and those from the original basis classes are denoted as different color crosses.

We observe that the blended microstructures are able to interpolate between – and in some cases, extend slightly beyond – basis classes in order to cover the property space. Although some sparse areas still exist due to the lower feasible bounds that we impose, this shows that blending is a powerful technique to create a large design space even with small sets of basis classes. It is also clear from these figures that the first basis (red) from both sets possess the highest stiffness in diagonal directions and ratios of C_{21}^H to C_{11}^H (equivalent to the effective Poisson’s ratio), as opposed to truss bases 4 (purple) and 5 (orange), and freeform basis 2 (blue), which are stiffest in uniaxial directions.

While the freeform classes are orthotropic, some of the truss classes are not. The number of responses in the neural networks of each set are adjusted accordingly, i.e., 6 elastic tensor components for trusses and 4 for freeform.

Table 1: Neural network architectures and accuracies.

	$n_{response}$	n_{node}	Train R^2	Val. R^2	Test R^2
Truss	6	$\{16,16,12\}$	0.9983	0.9984	0.9983
Freeform	4	$\{12,12,6\}$	0.9991	0.9990	0.9991

Val.: Validation.

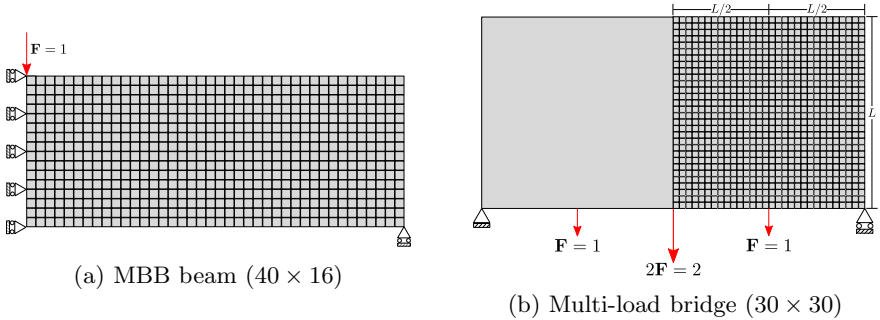
**Fig. 4:** Problem settings of the compliance minimization examples.

Table 1 lists the details of the ML model architectures, where n_{node} indicates the neurons of each hidden layer, and the R^2 metrics of the trained models. Since they only need to be built once, the same models are used for all examples throughout the paper.

The one-time expense of creating our data and models is reasonable for our 2D problems. However, we note that our results show overlapping properties in the dataset (Fig. 3c and f) and high R^2 values above 0.99 (Table 1), suggesting that it may not have been necessary to use as many samples as we did. There is great potential to develop adaptive sampling algorithms that better balance accuracy and efficiency, particularly for 3D and complex applications. We leave this for future works.

3.2 Compliance Minimization

We begin with compliance minimization examples, the first of which is the classic MBB beam, one of the most widespread validation problems in the TO field. The boundary conditions are depicted in 4a, and we follow the same set-up as in Xia and Breitkopf (2014) and Wang et al (2020c) in order to compare our results with those of existing methods. That is, the MBB beam is discretized into 40×16 microstructures and an ambitious global volume fraction limit is set as $V_{Global}^* = 0.36$. For the second problem, we pursue the same multi-load bridge as found in Wang et al (2020c), where a 60×30 structure is loaded in three places, as shown in Fig. 4b. Due to symmetry, we can cut its size by half into 30×30 . The target global volume there is $V_{Global}^* = 0.50$.

The two compliance problems can be formulated as:

$$\begin{aligned}
& \underset{\mathbf{c}, \mathbf{v}, \boldsymbol{\xi}, \mathbf{x}}{\text{minimize}} && f = f_c + kf_{div}(\mathbf{c}), \\
& \text{subject to} && \mathbf{KU} = \mathbf{F}, \\
& && g_1 = V_{Global}/V_{Global}^* - 1 \leq 0, \\
& && g_2 = V_{BESO}/V_{BESO}^* - 1 \leq 0,
\end{aligned} \tag{13}$$

where $f_c = \sum_{e=1}^{N_{el}} \mathbf{u}_e^T \mathbf{k}_e^H(\hat{\mathbf{c}}_e, \hat{v}_e) \mathbf{u}_e$ is the compliance with element displacements \mathbf{u}_e and effective stiffness matrices \mathbf{k}_e^H , which are predicted via the DL models. The global and macroscale volumes are $V_{Global} = \sum_{e=1}^{N_{el}} x_e \hat{v}_e / N_{el}$ and $V_{BESO} = \sum_{e=1}^{N_{el}} x_e / N_{el}$, respectively, and the bounds on the design variables are the same as described in Eq. 9. The sensitivities of this optimization problem are detailed in Appendix B.

For both examples, we initialize the volume constraints as $V_{Global,0}^* = 0.95$, $V_{BESO,0}^* = \sqrt{V_{Global}^*}$, the volumes \mathbf{v} as 0.95, the class weights so that $\tilde{\mathbf{c}}^{(m)}$ are the same, and all distribution fields, $\boldsymbol{\xi}^{(m)}$, so that the classes are distributed equally. The penalty parameter (Sec. 2.3.1) is set so that $kf_{div} = 10$ during later iterations. We find that keeping the penalty around this value improves both convergence and design performance.

The fixed parameters in the shape blending scheme are $\beta_1 = 64$ and $\beta_2 = 32$. As we suggested in Sec. 2.1.2, the threshold η_2 is adapts to the design and is equal to the 75th-percentile of the class weights. The radii of all filters on the design variables are the same, $r_{min} = 3.0$, matching [Xia and Breitkopf \(2014\)](#). For BESO, the evolutionary rate is $ER = 0.05$ in both problems. Otherwise, all other parameters are kept at the default values ([Huang and Xie, 2007](#); [Svanberg, 1987](#)). Our convergence criteria are when the change in design or the mean change in the objective over 10 iterations are less than 0.01, or when the number of iterations reaches 200. We also use early-stopping if the target V_{Global}^* has been met but the objective has not improved in 20 iterations.

3.2.1 2-Class Results with Different Basis Classes

We first consider the results using $M = 2$ new classes and both sets of basis classes. The optimal designs are shown in Figs. 5 and 6 for the MBB beam with truss and freeform bases, respectively, and in Figs. 7 and 8 for the multi-load bridge. The left side of the figures illustrate how the optimized classes are created via blending by breaking them down into the individual basis classes. For ease of interpretation, we show $\tilde{c}_d^{(m)}$ from Eq. 6, which correspond directly to the weights used during blending (Eq. 8), instead of the design variables $c_d^{(m)}$. The right-most sides of the figures present the optimal multiclass FGS and their final compliance, which are calculated by homogenizing each microstructure after the design is completed rather than using data-driven models.

From the 2-class compliance results, we can see several benefits of integrating multiclass shape blending into FGS design:

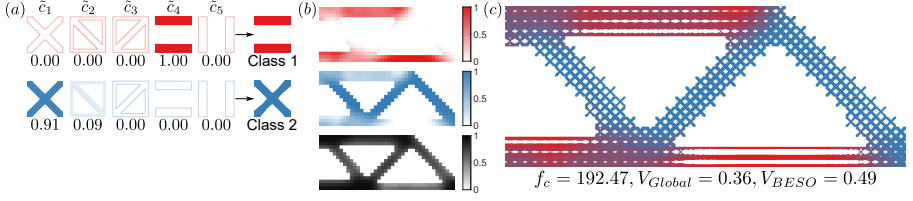


Fig. 5: Truss MBB, 2-class result. (a) Optimal new classes each drawn in a different color. Left of arrows: optimal weights listed under each basis. Lighter colors indicate low weights while outlined shapes represent weights that are zero. Right of arrows: representative topologies of new classes. (b) $\hat{\xi}^{(1)}$, $\hat{\xi}^{(2)}$, \hat{v} from top to bottom, and (c) multiclass FGS.

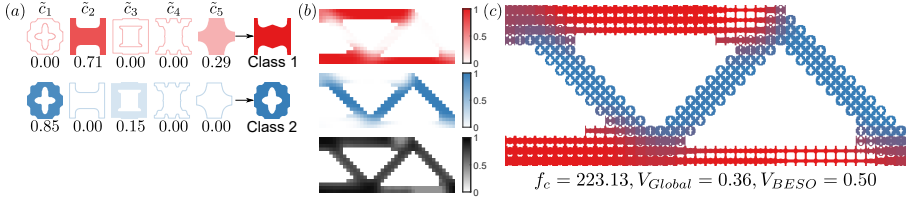


Fig. 6: Freeform MBB, 2-class result: optimal (a) weights and representatives of new classes, (b) $\hat{\xi}^{(1)}$, $\hat{\xi}^{(2)}$, \hat{v} from top to bottom, (c) multiclass FGS.

1. The combination of the blending scheme and the radial filters on the distribution fields creates smooth transitions between classes. Topological functional grading is guaranteed and does not depend on the mutual compatibility of the basis classes. Although connections may not be ideal for our freeform bases, which have low initial connectivity and more complex features, neighboring microstructures change continuously and are at least connected through the imposed lower feasible bounds (Fig. 6).
2. Because of the two-step blending scheme, the microstructures at the interfaces of optimized classes are a union of the classes being mixed there, and the minimum feature sizes of all microstructures match our prescribed lower limit of 4 pixels.
3. The macroscale distributions, $\hat{\xi}^{(m)}$, can be either dominated solely by one class or contain mixtures of multiple classes. For example, the diagonal struts in the truss MBB (Fig. 5a) consist predominantly of the second new class (blue), while the horizontal bars contain both (red and blue), presumably to stiffen the design at those locations. On the contrary, the two new classes in the freeform multi-load bridge intermingle throughout nearly the entire structure (Fig. 8).
4. Optimizing $c_d^{(m)}$ can automatically determine if an existing basis class is sufficient to achieve low compliance, or if a novel class needs to be created by fusing several bases. For example, in the freeform MBB result (Fig. 6), the mixture of the second and fifth bases stiffens the microstructures, improving the global compliance of the FGS.

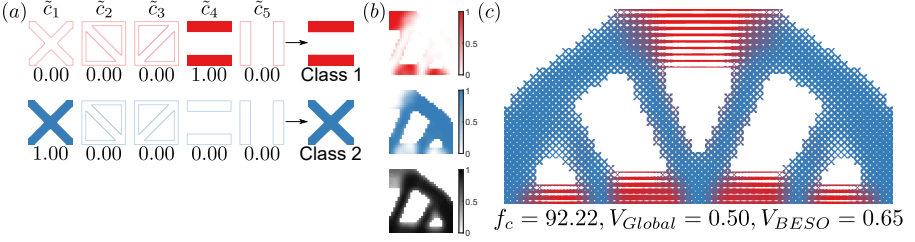


Fig. 7: Truss bridge, 2-class result: optimal (a) weights and representatives of new classes, (b) $\hat{\xi}^{(1)}$, $\hat{\xi}^{(2)}$, \hat{v} from top to bottom, (c) multiclass FGS reflected over the symmetry line.

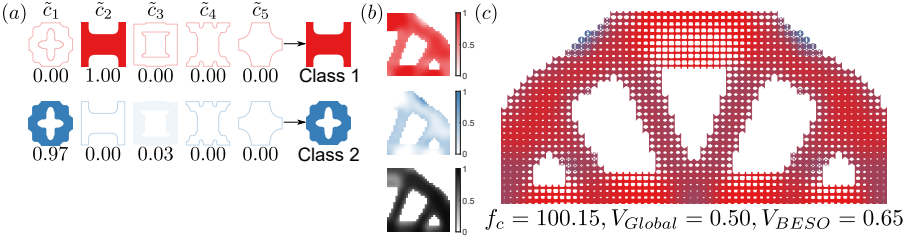


Fig. 8: Freeform bridge, 2-class result: optimal (a) weights and representatives of new classes, (b) $\hat{\xi}^{(1)}$, $\hat{\xi}^{(2)}$, \hat{v} from top to bottom, (c) multiclass FGS reflected over the symmetry line.

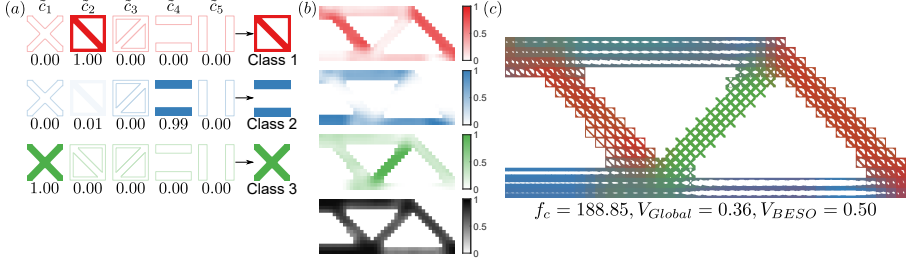
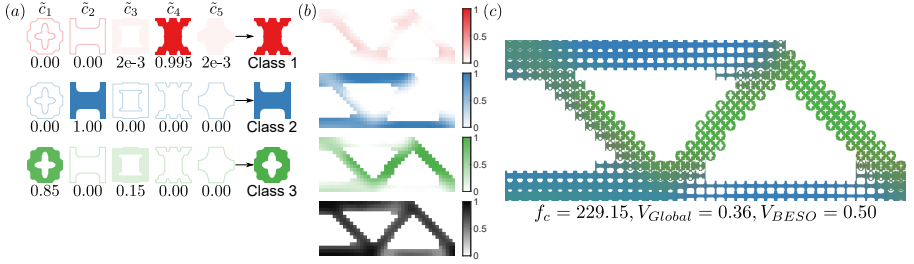
5. Due to BESO, the global macrostructures are clearly defined and change based on the basis classes and optimal microstructures, showing that the hybrid framework works well.

Further observations can be made regarding the framework’s ability to adapt to spatially-varying stress distributions. The first and fourth truss-type bases, and the first and second for freeform, are the most popular classes by far, agreeing with our observation in Sec. 3.1.3 that these are among the strongest classes in diagonal and uniaxial directions. In both beam and bridge examples, these classes are designed such that the load-bearing features of the blended microstructures intuitively match the load paths.

In particular, our truss-type MBB beam result is akin to those in existing multiscale works with the same design domain. [Xia and Breitkopf \(2014\)](#) performed an exhaustive two-scale TO that optimized every microstructure, resulting in horizontal (uniaxial) and diagonal (anisotropic) features that are oriented with stress directions, and a compliance of $f_c = 190$. Meanwhile, [Wang et al \(2020c\)](#) proposed a multiclass design with rectangular trusses on the horizontal macro-bars, X’s on the diagonal macro-struts, and a compliance of $f_c = 214.02$. Our framework can be thought of as bridging these two methods. This is indeed reflected in our 2-class truss result, which achieves a compliance value between the two existing works, $f_c = 192.47$, and has similar microstructures.

Table 2: Single-class MBB beam results using one freeform basis class each.

Basis	1	2	3	4	5
f_c	476.26	247.57	384.89	399.29	290.75


Fig. 9: Truss MBB, 3-class result: optimal (a) weights and representatives of new classes, (b) $\hat{\xi}^{(1)}$, $\hat{\xi}^{(2)}$, $\hat{\xi}^{(3)}$, $\hat{\mathbf{v}}$ from top to bottom, (c) multiclass FGS.

Fig. 10: Freeform MBB, 3-class result: optimal (a) weights and representatives of new classes, (b) $\hat{\xi}^{(1)}$, $\hat{\xi}^{(2)}$, $\hat{\xi}^{(3)}$, $\hat{\mathbf{v}}$ from top to bottom, (c) multiclass FGS.

In terms of performance, truss basis classes outshine the freeform basis in both problems. We theorize that our freeform bases do not perform as well for two reasons. (1) They were automatically chosen to maximize diversity, i.e., coverage, in shapes and properties, which undoubtedly can skip microstructures with properties that are more optimal for compliance. (2) They contain complex, thin features that force their lower feasible bounds to have high volume fractions ($v_{min} = 0.28$), which clashes with the low target volume of 0.36 in the MBB problem.

Despite these disadvantages, however, the compliance attained by using freeform basis classes is decent across both examples and near those of existing works, confirming the versatility of diverse bases and our design framework. In fact, for the multi-load bridge, the freeform set reaches $f_c = 100.15$, lower than the one in Wang et al (2020c), $f_c = 114.17$. A deeper look into the MBB example also reveals that the multiclass freeform FGS (Fig. 6) still surpasses single-class designs that vary only in volume fraction (Table 2).

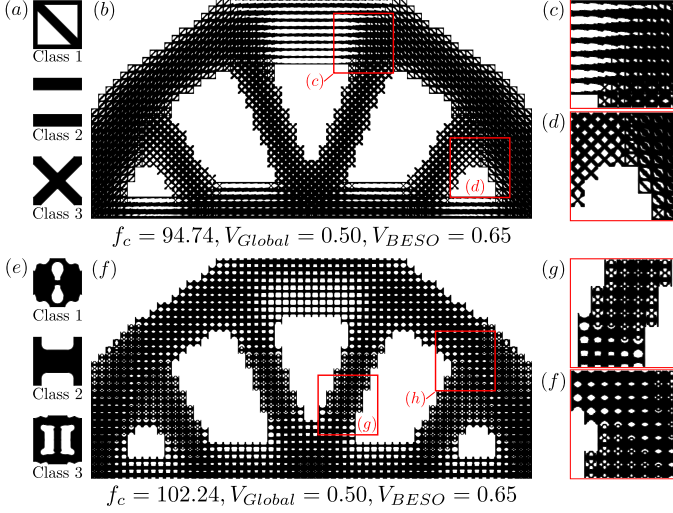


Fig. 11: Results of 3-class multi-load bridge in black-and-white. For truss bases: (a) optimal classes, (b) FGS, and (c,d) zoom-in views. For freeform bases: (e) optimal classes, (f) FGS, and (g,h) zoom-in views.

3.2.2 Effect of the Number of New Classes

With the effectiveness of the proposed framework established, we now study whether increasing the number of new classes to $M = 3$ can impact the designs and their performances. The problem definitions remain the same as before. For the MBB beam, the 3-class results are given in Figs. 9 and 10 with the truss and freeform bases, respectively. The multi-load results for both sets of bases are combined in Fig. 11, where they are shown in black-and-white and with zoomed-in views of the functionally graded topologies and volume fractions.

The most notable result is the 3-class truss MBB, which achieves a compliance even lower than the fully optimized design of Xia et al. at $f_c = 188.85$. More apparent than in the 2-class result above, it exhibits directional load-bearing features (Fig. 9) such as the left-to-right diagonal microstructures (red) and the near-uniaxial microstructures (blue). In addition, the X-shaped class (green) appears mainly in the middle macro-strut. Overall, our result distinguishes itself from the existing with the mix of isotropic and anisotropic microstructures that are all well-connected. A similar blend of directional and uniaxial classes can be found in our 3-class truss bridge (Fig. 11a-d), which also achieves a lower compliance than the design with the same discretization in Wang et al (2020c).

With the exception of the truss-type MBB, however, all 3-class results could not overtake the compliance of their 2-class counterparts. We suspect this is because, for simple compliance problems, additional classes are not necessary to achieve optimal performance. Our hypothesis is supported by the

Table 3: MBB beam results without penalty on low class diversity ($k = 0$). The dominant weights of each new class, $\tilde{\mathbf{c}}_m$, are **bolded**.

Basis	M	$\tilde{\mathbf{c}}_m$	f_c	V_{Global}	V_{BESO}
Truss	2	$\tilde{\mathbf{c}}_1 = [0.00, \mathbf{0.39}, 0.00, 0.27, 0.33]$ $\tilde{\mathbf{c}}_2 = [0.00, 0.05, 0.11, \mathbf{0.84}, 0.00]$	205.77	0.36	0.50
	3	$\tilde{\mathbf{c}}_1 = [0.00, \mathbf{0.36}, 0.22, 0.12, 0.30]$ $\tilde{\mathbf{c}}_2 = [0.12, 0.12, 0.09, \mathbf{0.66}, 0.01]$ $\tilde{\mathbf{c}}_3 = [0.23, 0.08, 0.16, \mathbf{0.53}, 0.01]$	212.83	0.36	0.54
Freeform	2	$\tilde{\mathbf{c}}_1 = [0.00, 0.09, 0.00, 0.00, \mathbf{0.91}]$ $\tilde{\mathbf{c}}_2 = [0.04, 0.14, 0.39, 0.01, \mathbf{0.43}]$	252.02	0.36	0.51
	3	$\tilde{\mathbf{c}}_1 = [0.01, 0.00, \mathbf{0.53}, 0.00, 0.46]$ $\tilde{\mathbf{c}}_2 = [0.00, 0.45, 0.00, 0.00, \mathbf{0.55}]$ $\tilde{\mathbf{c}}_3 = [0.00, 0.00, 0.00, 0.00, \mathbf{1.00}]$	248.84	0.36	0.50

new classes of the $M = 2$ examples: for the most part, they are each monopolized by just one basis class. This suggests that, in most cases, only two basis classes are needed throughout the entire FGS; if more are required, they can be incorporated into a single optimal class by adjusting the values of $\mathbf{c}^{(m)}$ without increasing M , like in the 2-class freeform MBB (Fig. 6). Another reason could be that we force the third class to be different from the others through the penalty on low diversity, which can lead to the addition of a sub-optimal class. It is possible that this scenario occurred in the 3-class freeform MBB, where the first new class (red) is hardly present in the FGS. Nevertheless, the penalty does not significantly worsen the compliance and can, in some cases improve it.

3.2.3 Effect of the Low-Diversity Penalty

As we showed, the function that penalizes new classes with low diversity (Eq. 10, Sec. 10) can affect performance, although whether that effect is positive or negative depends on the problem or basis classes. In this section, we show concrete examples why the penalty is still recommended by running the same compliance problems without the penalty, i.e., by setting $k = 0$. The results are listed in Tables 3 and 4. Immediately, we can see that although the truss basis classes can still achieve satisfactory compliance values lower than the existing baselines (Xia and Breitkopf, 2014; Wang et al, 2020c), none of these can beat our results above.

In the tables, we write the highest weight values of each new class, $\tilde{\mathbf{c}}_m$, in bold. From this, we observe that each result is often overshadowed by one basis class (see the bold values in the same column). For the 3-class designs in particular, the second and third new classes are always dominated by the same basis, confirming our earlier suspicion that $M = 2$ is enough to produce optimal

Table 4: Multi-load bridge results without penalty on low diversity ($k = 0$). The dominant weights of each new class, $\tilde{\mathbf{c}}_m$, are **bolded**.

Basis	M	$\tilde{\mathbf{c}}_m$	f_c	V_{Global}	V_{BESO}
Truss	2	$\tilde{\mathbf{c}}_1 = [0.00, 0.22, 0.00, \mathbf{0.73}, 0.05]$	96.59	0.50	0.65
		$\tilde{\mathbf{c}}_2 = [0.00, 0.41, 0.00, 0.09, \mathbf{0.51}]$			
	3	$\tilde{\mathbf{c}}_1 = [0.00, 0.18, 0.00, \mathbf{0.82}, 0.00]$ $\tilde{\mathbf{c}}_2 = [0.00, 0.28, 0.00, 0.21, \mathbf{0.51}]$ $\tilde{\mathbf{c}}_3 = [0.00, 0.45, 0.00, 0.00, \mathbf{0.54}]$	96.34	0.50	0.65
Freeform	2	$\tilde{\mathbf{c}}_1 = [0.00, 0.00, 0.13, \mathbf{0.87}, 0.00]$	105.90	0.50	0.65
		$\tilde{\mathbf{c}}_2 = [0.03, 0.00, 0.06, \mathbf{0.91}, 0.00]$			
	3	$\tilde{\mathbf{c}}_1 = [0.00, 0.00, 0.10, \mathbf{0.90}, 0.00]$ $\tilde{\mathbf{c}}_2 = [0.00, 0.00, 0.09, \mathbf{0.91}, 0.00]$ $\tilde{\mathbf{c}}_3 = [0.02, 0.00, 0.02, \mathbf{0.96}, 0.00]$	105.46	0.50	0.65

results. We also note that there are numerous low values of $\tilde{\mathbf{c}}_m$, signifying that multiple basis classes are being blended into the FGS without improving the design performance. These results additionally imply that greater diversity amongst the microstructure classes improves performance. A more meticulous study on the impact of diversity on the generality and performance of design methods is an intriguing path for future works.

Furthermore, it takes significantly longer for the class design variables to converge without penalization. In the 2-class truss bridge example without the penalty, they often fluctuate and need more than 100 iterations to start converging, whereas they are already converged in under 30 iterations with penalization. These studies validate the benefits that our proposed low-diversity penalty function supply to MMA, helping it to stabilize and find more optimal solutions. It is possible that another optimizer, such as globally-convergent MMA (Svanberg, 2002), could alleviate these issues but such an investigation is outside the current scope of this work.

3.3 Shape Matching

Heterogeneous structures show great potential for applications where a specific deformation pattern is desired upon actuation, e.g., in form-fitting wearables and soft robots (Mirzaali et al, 2018; Lumpe and Shea, 2021; Boley et al, 2019). Motivated by these applications, we optimize two shape matching structures: (1) the target sine-wave deformation profile shown in Fig. 12a, and (2) the bump profile in Fig. 12b. The first is a cantilever discretized into 30×4 microstructures, fixed at its left side and loaded with displacement boundary conditions on the right – the same example we tested in (Chan et al, 2020). The

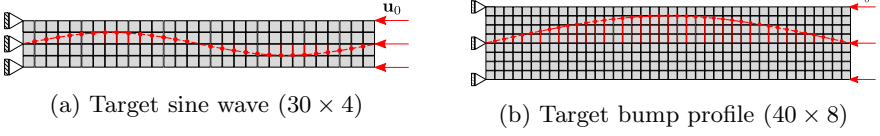


Fig. 12: Problem settings of the shape matching examples.

second is similar, but discretized into 40×8 . Like the compliance examples, we will also use the truss and freeform basis classes with $M = \{2, 3\}$.

In past works (Chan et al, 2020; Wang et al, 2020a), we found that these target displacement problems are similar to compliant mechanism design and most effectively solved via a two-stage "top-down" approach that first utilizes inverse TO to find the target effective properties for each microstructure. Departing from previous works, we use the proposed multiclass blending framework in the second stage to optimize the new classes, $\mathbf{c}^{(m)}$, their distributions, $\boldsymbol{\xi}^{(m)}$, and the volume fractions, \mathbf{v} , until the target properties are matched.

To find the target properties, i.e., the effective stiffness matrices \mathbf{C}_t^H , that achieve a desired displacement profile, the first stage follows the method in Wang et al (2020b) with following problem:

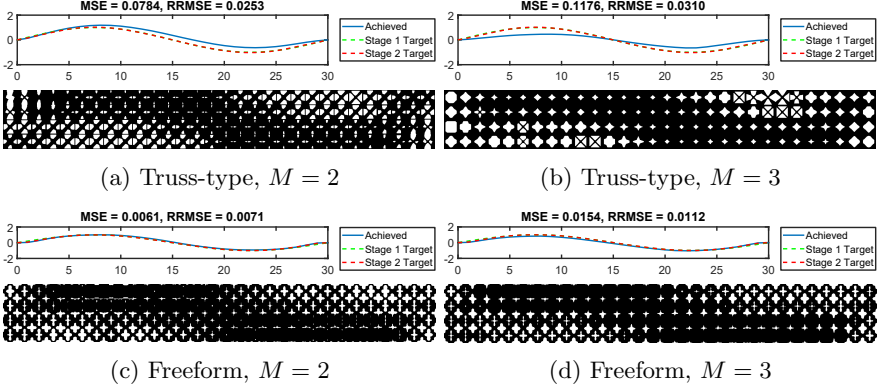
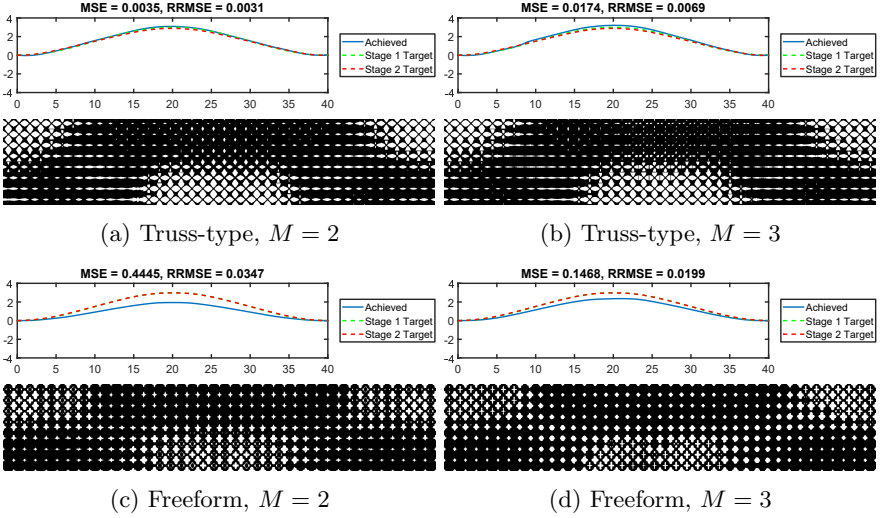
$$\begin{aligned}
 & \underset{\mathbf{C}_t^H}{\text{minimize}} && \frac{1}{n} \|\mathbf{u} - \mathbf{u}_t\|_2^2, \\
 & \text{subject to} && \mathbf{K}\mathbf{U} = \mathbf{F}, \\
 & && -\phi(\mathbf{C}_t^H) \leq 0,
 \end{aligned} \tag{14}$$

where \mathbf{u} is the displacement vector of n nodes located on the horizontal center-line of the structure, \mathbf{u}_t is the vector of target displacements of the same nodes, \mathbf{K} is the global stiffness matrix, and \mathbf{U} and \mathbf{F} are global displacement and loading vectors, respectively. This inverse problem uses the stiffness matrices of each microstructure as design variables. To ensure that these are within the bounds attainable by shape blending, they are constrained by the signed L_2 distance field ϕ of the properties of the training data for the neural networks (Sec. 2.2 and Fig. 3c and f).

After this, the multiclass FGS is optimized to meet the effective property targets by leveraging our proposed blending scheme. Since we do not aim for a target volume here, there is no global volume constraint and the macrostructure defined by \mathbf{x} remains fixed. The second stage of optimization is thus:

$$\begin{aligned}
 & \underset{\mathbf{c}, \mathbf{v}, \boldsymbol{\xi}}{\text{minimize}} && \frac{1}{N_{el}} \|\mathbf{C}^H(\mathbf{c}, \mathbf{v}, \boldsymbol{\xi}) - \mathbf{C}_t^H\|_2^2 + kf_{div}(\mathbf{c}), \\
 & \text{subject to} && \mathbf{K}\mathbf{U} = \mathbf{F},
 \end{aligned} \tag{15}$$

where the bounds on the design variables are the same as in the previous examples. Due to the omission of \mathbf{x} , it can be solved with just MMA. For the 2-class examples, the penalization parameter is set such that $kf_{div} = 4$ in the

**Fig. 13:** Results of the target sine wave problem.**Fig. 14:** Results of the target bump shape example.

final iterations, while it is $k_{div} = 9$ for the 3-class studies. The filter radius is $r_{min} = 1.2$ and $r_{min} = 2.5$ for the sine and bump problems, respectively. The volume fractions are initialized at $\mathbf{v} = 0.5$ in every case, and all other parameters are the same as in the compliance examples.

The final multiclass FGS and their achieved displacement profiles (solid blue) are gathered in Fig. 13 for the sine wave and Fig. 14 for the bump problem. In the plots of the displacements, we also show the initial target profile, \mathbf{u}_t , used in stage one in dashed green lines, along with profile realized by the optimized properties (dashed red), which serves as an indirect target profile in the second stage.

We performed the same sine wave study in [Chan et al \(2020\)](#), but with a combinatorial method for aperiodic designs, i.e., without functional grading. There, the lowest MSE that we achieved was 0.1146, which most of our proposed multiclass FGS surpass. Interestingly, the freeform basis classes perform considerably better than the truss-types. The freeform designs are composed mostly of the first basis, which we noted in [Sec. 3.1.3](#) has one of the greatest effective Poisson’s ratios, as well as the fifth freeform basis, which has both high stiffness and medium Poisson’s ratio.

Conversely, the truss-type FGS match the target bump profile more closely than the freeform ones by utilizing the fourth (horizontal) truss basis. By inspecting the target properties for each problem, we find that the sine wave requires middling values of both Poisson’s ratio and stiffness throughout the FGS, which the freeform classes provide more easily, whereas the bump profile needs distinct regions of either large x -directional stiffness or high Poisson’s ratio, which the first and fourth truss classes meet exceptionally well (see [Fig. 3c](#) and [f](#)). This observation portends a possible extension of our work where the most efficient basis classes can be chosen to match the distribution of principal macroscale stresses for specific problems, similar to the clustering method in [Qiu et al \(2020\)](#).

Another intriguing note is that, by blending the last two truss basis classes, we can form square microstructures that are not found in the original set ([Fig. 13b](#)). Moreover, combining those two with the ‘X’ basis creates microstructures with star-shaped voids that are not strictly trusses. These are direct results of the weighted sum of SDFs in our proposed blending scheme ([Eq. 3](#)), which can non-intuitively morph the basis classes to achieve optimal performance.

4 Conclusions

We proposed in this work a novel multiclass shape blending scheme that provides a low-dimensional representation of microstructures for both design and DL, and a data-driven multiscale design method that utilizes a hybrid of TO algorithms along with a new penalty on low diversity designs. By integrating these, we created a multiclass FGS design framework that encapsulates the freedom of fully aperiodic structures while featuring efficiency greater than that of typical multiscale methods. The key is the ability of shape blending to blur the lines between classes, creating graded designs with novel microstructures beyond the initial basis classes. Even with classes that are not mutually compatible or have complex features, continuous transitions between neighboring microstructures are guaranteed.

Furthermore, feasibility constraints are incorporated into the scheme to ensure that they are naturally met. In this work, we use a simple measure – minimum feature size. However, defining the lower feasible bounds of each basis class outside of the optimization process means there is potential for future

works to incorporate other feasibility, or even quality, metrics, such as those without cheap or tractable gradients.

We demonstrated these advantages through compliance and shape matching examples, in which blending empowered our FGS to surpass designs in literature. Our results revealed that truss-type classes consistently achieve low compliance, and that diverse freeform classes reach satisfactory performance across multiple applications despite being automatically chosen without considering their compatibility. We also discovered that more is not always better when it comes to classes. By encouraging the design to converge to a smaller number of diverse classes, as few as two can be blended to obtain optimal designs. This outcome merits deeper exploration in the future on how diversity metrics can benefit structural design.

Our framework is general in that it is not tied to the specific DL and TO methods shown in this work. It is also not limited to our 2D classes, since multiclass blending is independent of the topology, representation, dimension and resolution of the basis shapes. This modularity is an especially welcome feature as more advanced prediction models and TO algorithms emerge to solve complex multiphysics and nonlinear mechanics problems, including 3D ones. Beyond the examples presented, our framework can be extended to sought-after functionalities like thermoelasticity, fracture resistance and energy absorption, and adapted to applications such as customized user products and architectural design. We believe these are all exciting avenues for future works enabled by multiclass shape blending.

Acknowledgements

We are grateful for the MMA codes from Prof. K. Svanberg at the Royal Institute of Technology, and the BESO codes from Profs. X. Huang and Y. M. Xie at RMIT University.

Funding information

The authors were supported by the National Science Foundation (NSF) CSSI program (Grant No. OAC-1835782). Yu-Chin Chan received funding from the NSF Graduate Research Fellowship (Grant No. DGE-1842165), and Liwei Wang from the Zhiyuan Honors Program for Graduate Students of Shanghai Jiao Tong University for his predoctoral visit at Northwestern University.

Conflict of interest

The authors declare that they have no conflict of interest.

Replication of results

All proposed schemes and algorithms are disclosed within this paper and developed by the authors in MATLAB (multiclass shape blending scheme, concurrent design, and dataset generation) and Python (pre-processing of basis classes). The deep learning models are implemented with the Deep Learning Toolbox in MATLAB. Additional codes are adapted from open-source packages and are cited. The dataset from which the diverse freeform basis classes are extracted can be found at <https://ideal.mech.northwestern.edu/>.

References

- (2021) scikit-fmm: the fast marching method for python. <https://github.com/scikit-fmm/scikit-fmm>
- Andreasen CS, Elingaard MO, Aage N (2020) Level set topology and shape optimization by density methods using cut elements with length scale control 62(2):685–707. <https://doi.org/10.1007/s00158-020-02527-1>
- Andreassen E, Andreasen CS (2014) How to determine composite material properties using numerical homogenization. *Computational Materials Science* 83:488–495. <https://doi.org/10.1016/j.commatsci.2013.09.006>
- Ba S, Myers WR, Brenneman WA (2015) Optimal sliced latin hypercube designs. *Technometrics* 57(4):479–487. <https://doi.org/10.1080/00401706.2014.957867>
- Bendsøe MP, Sigmund O (2004) *Topology Optimization*. Springer Berlin Heidelberg, <https://doi.org/10.1007/978-3-662-05086-6>
- Bojsen-Hansen M, Li H, Wojtan C (2012) Tracking surfaces with evolving topology 31(4):1–10. <https://doi.org/10.1145/2185520.2185549>
- Boley JW, van Rees WM, Lissandrello C, et al (2019) Shape-shifting structured lattices via multimaterial 4d printing. *Proceedings of the National Academy of Sciences* 116(42):20,856–20,862. <https://doi.org/10.1073/pnas.1908806116>
- Boyd S, Vandenberghe L (2004) *Convex Optimization*. Cambridge University Press, Cambridge, <https://doi.org/10.1017/cbo9780511804441>
- Breen D, Whitaker R (2001) A level-set approach for the metamorphosis of solid models 7(2):173–192. <https://doi.org/10.1109/2945.928169>
- Carballido-Gamio J, Bauer J, Lee KY, et al (2005) Combined image processing techniques for characterization of MRI cartilage of the knee. *IEEE*, <https://doi.org/10.1109/iembs.2005.1617116>

- Chan YC, Shintani K, Chen W (2019) Robust topology optimization of multi-material lattice structures under material and load uncertainties. *Frontiers of Mechanical Engineering* 14(2):141–152. <https://doi.org/10.1007/s11465-019-0531-4>
- Chan YC, Ahmed F, Wang L, et al (2020) METASET: Exploring shape and property spaces for data-driven metamaterials design. *Journal of Mechanical Design* 143(3). <https://doi.org/10.1115/1.4048629>
- Christiansen AN, Nobel-Jørgensen M, Aage N, et al (2013) Topology optimization using an explicit interface representation 49(3):387–399. <https://doi.org/10.1007/s00158-013-0983-9>
- Chu S, Gao L, Xiao M, et al (2019) Multiscale topology optimization for coated structures with multifarious-microstructural infill. *Structural and Multidisciplinary Optimization* 61(4):1473–1494. <https://doi.org/10.1007/s00158-019-02428-y>
- Coulais C, Teomy E, de Reus K, et al (2016) Combinatorial design of textured mechanical metamaterials. *Nature* 535(7613):529–532. <https://doi.org/10.1038/nature18960>
- Da D, Cui X, Long K, et al (2019) Multiscale concurrent topology optimization of structures and microscopic multi-phase materials for thermal conductivity. *Engineering Computations* 36(1):126–146. <https://doi.org/10.1108/ec-01-2018-0007>
- Da D, Chan YC, Wang L, et al (2021) Data-driven and topological design of structural metamaterials for fracture resistance. *Extreme Mechanics Letters* p 101528. <https://doi.org/10.1016/j.eml.2021.101528>
- Das S, Sutradhar A (2020) Multi-physics topology optimization of functionally graded controllable porous structures: Application to heat dissipating problems 193:108,775. <https://doi.org/10.1016/j.matdes.2020.108775>
- Deng J, Pedersen CBW, Chen W (2019) Connected morphable components-based multiscale topology optimization 14(2):129–140. <https://doi.org/10.1007/s11465-019-0532-3>
- Du Z, Zhou XY, Picelli R, et al (2018) Connecting microstructures for multiscale topology optimization with connectivity index constraints. *Journal of Mechanical Design* 140(11). <https://doi.org/10.1115/1.4041176>
- Eisenberger M, Löhner Z, Cremers D (2019) Divergence-free shape correspondence by deformation. *Computer Graphics Forum* 38(5):1–12. <https://doi.org/10.1111/cgf.13785>

- Ferrer A, Cante J, Hernández J, et al (2018) Two-scale topology optimization in computational material design: An integrated approach. *International Journal for Numerical Methods in Engineering* 114(3):232–254. <https://doi.org/10.1002/nme.5742>
- Garner E, Kolken HM, Wang CC, et al (2019) Compatibility in microstructural optimization for additive manufacturing. *Additive Manufacturing* 26:65–75. <https://doi.org/10.1016/j.addma.2018.12.007>
- Gavin HP (2019) The levenberg-marquardt algorithm for nonlinear least squares curve-fitting problems
- Gu J, Li Z, Wang Y, et al (2019) Deep generative adversarial networks for thin-section infant MR image reconstruction. *IEEE Access* 7:68,290–68,304. <https://doi.org/10.1109/access.2019.2918926>
- Hastie T, Tibshirani R, Friedman J (2009) *The Elements of Statistical Learning*. Springer New York, <https://doi.org/10.1007/978-0-387-84858-7>
- Huang X, Xie Y (2007) Convergent and mesh-independent solutions for the bi-directional evolutionary structural optimization method. *Finite Elements in Analysis and Design* 43(14):1039–1049. <https://doi.org/10.1016/j.finel.2007.06.006>
- Jansen M, Pierard O (2020) A hybrid density/level set formulation for topology optimization of functionally graded lattice structures. *Computers & Structures* 231:106,205. <https://doi.org/10.1016/j.compstruc.2020.106205>
- Jia J, Da D, Hu J, et al (2021) Crashworthiness design of periodic cellular structures using topology optimization. *Composite Structures* 271:114,164. <https://doi.org/10.1016/j.compstruct.2021.114164>
- Kumar S, Tan S, Zheng L, et al (2020) Inverse-designed spinodoid metamaterials. *npj Computational Materials* 6(1). <https://doi.org/10.1038/s41524-020-0341-6>
- Li D, Dai N, Tang Y, et al (2019) Design and optimization of graded cellular structures with triply periodic level surface-based topological shapes. *Journal of Mechanical Design* 141(7). <https://doi.org/10.1115/1.4042617>
- Liu H, Zong H, Tian Y, et al (2019) A novel subdomain level set method for structural topology optimization and its application in graded cellular structure design. *Structural and Multidisciplinary Optimization* 60(6):2221–2247. <https://doi.org/10.1007/s00158-019-02318-3>
- Lumpe TS, Shea K (2021) Computational design of 3d-printed active lattice structures for reversible shape morphing. *Journal of Materials Research*

<https://doi.org/10.1557/s43578-021-00225-2>

- Luo Y, Hu J, Liu S (2021) Self-connected multi-domain topology optimization of structures with multiple dissimilar microstructures. *Structural and Multidisciplinary Optimization* 64(1):125–140. <https://doi.org/10.1007/s00158-021-02865-8>
- Mirzaali MJ, Janbaz S, Strano M, et al (2018) Shape-matching soft mechanical metamaterials. *Scientific Reports* 8(1). <https://doi.org/10.1038/s41598-018-19381-3>
- Oring A, Yakhini Z, Hel-Or Y (2020) Autoencoder image interpolation by shaping the latent space. [2008.01487](https://arxiv.org/abs/2008.01487)
- Panesar A, Abdi M, Hickman D, et al (2018) Strategies for functionally graded lattice structures derived using topology optimisation for additive manufacturing. *Additive Manufacturing* 19:81–94. <https://doi.org/10.1016/j.addma.2017.11.008>
- Panetta J, Zhou Q, Malomo L, et al (2015) Elastic textures for additive fabrication. *ACM Transactions on Graphics (TOG)* 34(4):1–12. <https://doi.org/10.1145/2766937>
- Qiu Z, Li Q, Liu S, et al (2020) Clustering-based concurrent topology optimization with macrostructure, components, and materials. *Structural and Multidisciplinary Optimization* 63(3):1243–1263. <https://doi.org/10.1007/s00158-020-02755-5>
- Ricci A (1973) A constructive geometry for computer graphics 16(2):157–160. <https://doi.org/10.1093/comjnl/16.2.157>
- Rohra AI, Kulkarni RK (2019) Survey on recent trends in image morphing techniques. In: 2019 International Conference on Smart Systems and Inventive Technology (ICSSIT). IEEE, <https://doi.org/10.1109/icssit46314.2019.8987879>
- Sanchez M (2016) Distance based heterogeneous volume modelling. PhD thesis
- Sanchez M, Fryazinov O, Adzhiev V, et al (2015) Space-time transfinite interpolation of volumetric material properties. *IEEE Transactions on Visualization and Computer Graphics* 21(2):278–288. <https://doi.org/10.1109/tvcg.2014.2356196>
- Sanders ED, Pereira A, Paulino GH (2021) Optimal and continuous multilattice embedding. *Science Advances* 7(16):eabf4838. <https://doi.org/10.1126/sciadv.abf4838>

- Schumacher C, Bickel B, Rys J, et al (2015) Microstructures to control elasticity in 3d printing. *ACM Transactions on Graphics (TOG)* 34(4):1–13. <https://doi.org/10.1145/2766926>
- Shapiro V (2007) Semi-analytic geometry with r-functions. *Acta Numerica* 16:239–303. <https://doi.org/10.1017/s096249290631001x>
- Sigmund O (2007) Morphology-based black and white filters for topology optimization 33(4-5):401–424. <https://doi.org/10.1007/s00158-006-0087-x>
- Smith H, Norato JA (2020) A MATLAB code for topology optimization using the geometry projection method. *Structural and Multidisciplinary Optimization* 62(3):1579–1594. <https://doi.org/10.1007/s00158-020-02552-0>
- Svanberg K (1987) The method of moving asymptotes—a new method for structural optimization. *International Journal for Numerical Methods in Engineering* 24(2):359–373. <https://doi.org/10.1002/nme.1620240207>
- Svanberg K (2002) A class of globally convergent optimization methods based on conservative convex separable approximations. *SIAM Journal on Optimization* 12(2):555–573. <https://doi.org/10.1137/s1052623499362822>
- Thomas AE, Guevelou S, Pasquale ED, et al (2020) Shape parametrization & morphing in sheet-metal forming. *Procedia Manufacturing* 47:702–706. <https://doi.org/10.1016/j.promfg.2020.04.216>
- Wang L, Chan YC, Ahmed F, et al (2020a) Deep generative modeling for mechanistic-based learning and design of metamaterial systems. *Computer Methods in Applied Mechanics and Engineering* 372:113,377. <https://doi.org/10.1016/j.cma.2020.113377>
- Wang L, Chan YC, Liu Z, et al (2020b) Data-driven metamaterial design with laplace-beltrami spectrum as “shape-DNA”. *Structural and Multidisciplinary Optimization* <https://doi.org/10.1007/s00158-020-02523-5>
- Wang L, Tao S, Zhu P, et al (2020c) Data-driven topology optimization with multiclass microstructures using latent variable gaussian process. *Journal of Mechanical Design* 143(3). <https://doi.org/10.1115/1.4048628>
- Wang Y, Zhang L, Daynes S, et al (2018) Design of graded lattice structure with optimized mesostructures for additive manufacturing. *Materials & Design* 142:114–123. <https://doi.org/10.1016/j.matdes.2018.01.011>
- Wu J, Sigmund O, Groen JP (2021) Topology optimization of multi-scale structures: a review. *Structural and Multidisciplinary Optimization* 63(3):1455–1480. <https://doi.org/10.1007/s00158-021-02881-8>

- Xia L, Breitkopf P (2014) Concurrent topology optimization design of material and structure within fe2 nonlinear multiscale analysis framework 278:524–542. <https://doi.org/10.1016/j.cma.2014.05.022>
- Zhang W, Yuan J, Zhang J, et al (2015) A new topology optimization approach based on moving morphable components (MMC) and the ersatz material model. *Structural and Multidisciplinary Optimization* 53(6):1243–1260. <https://doi.org/10.1007/s00158-015-1372-3>
- Zhang Y, Li H, Xiao M, et al (2018) Concurrent topology optimization for cellular structures with nonuniform microstructures based on the kriging metamodel 59(4):1273–1299. <https://doi.org/10.1007/s00158-018-2130-0>
- Zhou XY, Du Z, Kim HA (2019) A level set shape metamorphosis with mechanical constraints for geometrically graded microstructures. *Structural and Multidisciplinary Optimization* 60(1):1–16. <https://doi.org/10.1007/s00158-019-02293-9>
- Zhu B, Skouras M, Chen D, et al (2017) Two-scale topology optimization with microstructures. *ACM Transactions on Graphics* 36(4):1. <https://doi.org/10.1145/3072959.3095815>
- Zobaer SMT, Sutradhar A (2020) An energy-based method for interface connectivity of incompatible microstructures through parametric modeling. *Computer Methods in Applied Mechanics and Engineering* 370:113,278. <https://doi.org/10.1016/j.cma.2020.113278>
- Zong H, Liu H, Ma Q, et al (2019) VCUT level set method for topology optimization of functionally graded cellular structures. *Computer Methods in Applied Mechanics and Engineering* 354:487–505. <https://doi.org/10.1016/j.cma.2019.05.029>

Appendix A Algorithms

Algorithm 1 Adaptive scheme to decrease volume fraction limits during concurrent multiscale design. i denotes the number of the current iteration.

Require: $V_{Global,i-1}^*, V_{BESO,i-1}^*, V_{Global}, V_{BESO}$;

- 1: **if** $(i \bmod 10) = 0$ **and** $V_{Global,i-1}^* > V_{Global}^*$ **then**
- 2: $V_{Global,i}^* \leftarrow \min(V_{Global}, V_{Global,i-1}^*) - 0.025$;
- 3: **end if**
- 4: **if** $(i \bmod 10) = 0$ **and** $V_{BESO} \leq V_{BESO,i-1}^*$ **then**
- 5: $V_{BESO,i}^* \leftarrow V_{BESO,i-1}^* - 0.005$;
- 6: **end if**
- 7: **return** updated volume constraints.

Algorithm 2 Concurrent design framework for multiclass functionally graded structures. If there are no volume constraints, ignore Line 10. If the macrostructure is fixed, ignore Line 12.

- 1: **Initialize:**
 - design variables $\mathbf{c}, \mathbf{v}, \boldsymbol{\xi}, \mathbf{x}$;
 - volume constraints $V_{Global,0}^*, V_{BESO,0}^*$;
 - weight on low-diversity penalty k ;
- 2: **while** change in design $> tol$ **do**
- 3: $i \leftarrow i + 1$; \triangleright iteration counter
- 4: **for** each macro-element e **do**
- 5: obtain $\hat{\mathbf{c}}_e$ (Eqs. 6, 7);
- 6: find Φ_e and t_e so that unit cell has volume \hat{v}_e (Eq. 8);
- 7: approximate \hat{v}_e^a (Eqs. 11, 12);
- 8: predict effective stiffness $\mathbf{C}_e^H = NN(\bar{\mathbf{c}}_e, \hat{v}_e)$ and obtain \mathbf{k}_e ;
- 9: **end for**
- 10: update volume fraction constraint limits (Algorithm 1);
- 11: compute objective, constraints and sensitivities (Appendix B);
- 12: update macroscale design \mathbf{x} with BESO;
- 13: update other variables $\mathbf{c}, \mathbf{v}, \boldsymbol{\xi}$ with MMA;
- 14: **end while**
- 15: **return** optimal multiclass functionally graded design.

Appendix B Sensitivity Analysis

The derivations of the sensitivity analysis for gradient-based topology optimization (TO) are detailed in this section. The nomenclature are the same as in the main text, e.g., D is the number of basis classes, M is the number of new

classes to be optimized, N_{el} is the number of macro-elements (i.e., microstructures), and n_{el} is the number of micro-elements in each microstructure (in our case, 50×50). All derivations were verified using the finite difference method.

For the global multiclass shape blending scheme (Eq. 8), which is used to obtain the microscale topology at e , the gradient is

$$\frac{\partial \Phi_e}{\partial \hat{c}_{e,d}} = \frac{1}{\beta_2 \Phi_d^I} \left[\beta_2 \exp(\beta_2 \Phi_e^0) \odot \Phi_d^* + \frac{\partial H(\hat{c}_{e,d}, \beta_2, \eta_2)}{\partial \hat{c}_{e,d}} \exp(\beta_2 \Phi_d^L) \right], \quad (B1)$$

where

$$\Phi_e^I = \exp(\beta_2 \Phi_e^0) + \sum_d^D a_d \exp(\beta_2 \Phi_d^L), \quad (B2)$$

$$\Phi_e^0 = \sum_d^D \hat{c}_{e,d} \Phi_d^* + t_e, \quad (B3)$$

$$\frac{\partial H(\hat{c}_{e,d}, \beta_2, \eta_2)}{\partial \hat{c}_{e,d}} = \frac{\beta_2 [1 - \tanh^2(\beta_2(\hat{c}_{e,d} - \eta_2))]}{\tanh(\beta_2 \eta_2) + \tanh(\beta_2(1 - \eta_2))}, \quad (B4)$$

and \odot indicates element-wise multiplication.

The sensitivities for the the class interpolation schemes (Eqns. 6 and 7) with respect to the class design variables is as follows:

$$\frac{\partial \hat{c}_{e,d}}{\partial \tilde{c}_d^{(m)}} = \left\{ \frac{\partial \tilde{c}_d^{(1)}}{\partial \tilde{c}_d^{(m)}} + \sum_{j=1}^{M-1} \left[\frac{\partial(\tilde{c}_d^{(j+1)} - \tilde{c}_d^{(j)})}{\partial \tilde{c}_d^{(m)}} \prod_{k=1}^j \hat{\xi}_e^{(k)} \right] \right\} \frac{\partial \tilde{c}_d^{(m)}}{\partial c_d^{(m)}}, \quad (B5)$$

where

$$\frac{\partial \tilde{c}_d^{(m)}}{\partial c_d^{(m)}} = \sum_{j=d}^{D-1} \left[(z_d^{(j+1)} - z_d^{(j)}) \prod_{k=1, k \neq d}^j c_k^{(m)} \right]. \quad (B6)$$

With respect to the macroscale distribution fields, it is:

$$\frac{\partial \hat{c}_{e,d}}{\partial \xi_e^{(m)}} = \sum_{j=m}^{M-1} \left[(\tilde{c}_d^{(j+1)} - \tilde{c}_d^{(j)}) \prod_{k=1, k \neq m}^j \hat{\xi}_e^{(k)} \right] \frac{\hat{\xi}_e^{(m)}}{\xi_e^{(m)}}. \quad (B7)$$

We also need the sensitivities of the radial filters. This follows the traditional TO methods closely (Sigmund, 2007), and are defined by

$$\begin{aligned} \frac{\partial \hat{v}_e}{\partial v_e} &= \frac{w_e}{\sum_{i \in S_e} w_i}, \\ \frac{\partial \hat{\xi}_e^{(m)}}{\partial \xi_e^{(m)}} &= \frac{w_e}{\sum_{i \in S_e} w_i}. \end{aligned} \quad (B8)$$

S_e is the set of elements neighboring e , and the weighting function w_i is

$$w_i = \max(0, r_{min} - \|(\cdot)_i - (\cdot)_e\|_2), \quad (B9)$$

where (\cdot) is the appropriate variable, v or $\xi^{(m)}$, and r_{min} is the filter radius.

Using these, we can obtain the other sensitivities. For compliance (Eq. 13), the adjoint method (Bendsøe and Sigmund, 2004) and chain rule allow us to derive the following with respect to the design variables:

$$\frac{\partial f_c}{\partial c_{e,d}} = - \left[\sum_{n=1}^{N_{el}} \mathbf{u}_n^T \frac{\partial \mathbf{k}_n}{\partial \hat{c}_{e,d}} \mathbf{u}_n \right] \frac{\partial \hat{c}_{e,d}}{\partial c_{e,d}}, \quad (\text{B10})$$

$$\frac{\partial f_c}{\partial v_e} = - \left[\sum_{n=1}^{N_{el}} \mathbf{u}_n^T \frac{\partial \mathbf{k}_n}{\partial \hat{v}_e} \mathbf{u}_n \right] \frac{\partial \hat{v}_e}{\partial v_e}, \quad (\text{B11})$$

and

$$\frac{\partial f_c}{\partial \xi_e^{(m)}} = - \left[\sum_{n=1}^{N_{el}} \mathbf{u}_n^T \frac{\partial \mathbf{k}_n}{\partial \hat{\xi}_e^{(m)}} \mathbf{u}_n \right] \frac{\hat{\xi}_e^{(m)}}{\xi_e^{(m)}}. \quad (\text{B12})$$

The derivatives of the element effective stiffness matrices are

$$\frac{\partial \mathbf{k}_e}{\partial \hat{c}_{e,d}} = \frac{\partial \mathbf{k}_e}{\partial \mathbf{C}_e} \frac{\partial \mathbf{C}_e}{\partial \hat{c}_{e,d}}, \quad (\text{B13})$$

$$\frac{\partial \mathbf{k}_e}{\partial \hat{v}_e} = \frac{\partial \mathbf{k}_e}{\partial \mathbf{C}_e} \frac{\partial \mathbf{C}_e}{\partial \hat{v}_e}, \quad (\text{B14})$$

and

$$\frac{\partial \mathbf{k}_e}{\partial \hat{\xi}_e^{(m)}} = \frac{\partial \mathbf{k}_e}{\partial \mathbf{C}_e} \left[\sum_{d=1}^D \frac{\partial \mathbf{C}_e}{\partial \hat{c}_{e,d}} \frac{\partial \hat{c}_{e,d}}{\partial \hat{\xi}_e^{(m)}} \right]. \quad (\text{B15})$$

Here, due to our data-driven framework, the gradients of the effective properties $\partial \mathbf{C}_e / \partial \hat{c}_{e,d}$ and $\partial \mathbf{C}_e / \partial \hat{v}_e$ are obtained by backpropagating through the layers of the fully connected neural network (Hastie et al, 2009).

To obtain the sensitivities of the global volume fraction constraint, we can use Eq. B1 and the Sigmoid function (Eq. 11 in Sec. 2.3.2), which gives us a continuous approximation of a volume fraction (\hat{v}_e^a from Eq. 12). First, the derivative of the Sigmoid applied to a microstructure's SDF (Φ_e) is

$$\frac{\partial S(\Phi_e, \beta_1)}{\partial \Phi_e} = \beta_1 S(\Phi_e, \beta_1) (1 - S(\Phi_e, \beta_1)). \quad (\text{B16})$$

Therefore, the sensitivity of the global volume fraction can be decomposed as

$$\begin{aligned} \frac{\partial V_{Global}}{\partial \hat{c}_{e,d}} &= \frac{\partial V_{Global}}{\partial \hat{v}_e^a} \frac{\partial \hat{v}_e^a}{\partial S} \frac{\partial S}{\partial \Phi_e} \frac{\partial \Phi_e}{\partial \hat{c}_{e,d}}, \\ &= \frac{x_e}{N_{el}} \left(\frac{1}{n_{el}} \sum_{u=1}^{n_{el}} \frac{\partial S}{\partial \Phi_e} \right) \frac{\partial \Phi_e}{\partial \hat{c}_{e,d}}, \end{aligned} \quad (\text{B17})$$

and the sensitivities of the constraint itself with respect to the design variables are:

$$\frac{\partial g_1}{\partial c_{e,d}} = \frac{1}{V_{Global}^*} \frac{\partial V_{Global}}{\partial \hat{c}_{e,d}} \frac{\partial \hat{c}_{e,d}}{\partial c_{e,d}}, \quad (\text{B18})$$

$$\frac{\partial g_1}{\partial v_e} = \frac{1}{V_{Global}^*}, \quad (\text{B19})$$

and

$$\frac{\partial g_1}{\partial \xi_e^{(m)}} = \frac{1}{V_{Global}^*} \frac{\partial V_{Global}}{\partial \hat{c}_{e \cdot d}} \frac{\partial \hat{c}_{e \cdot d}}{\xi_e^{(m)}}. \quad (\text{B20})$$

We note that these approximations of the microstructural volume fractions do introduce some error into the sensitivities but, in our experience, are minor and not detrimental to the designs.

Since we use the default algorithm for BESO developed by [Huang and Xie \(2007\)](#) to update \mathbf{x} , the filtering of the macroscale sensitivity numbers for the compliance problems can be found in the original paper. The only difference is that, instead of the element stiffness for a homogeneous material, we use the effective stiffness predicted by the data-driven models. Thus, our sensitivity numbers are modified to be

$$\alpha_e = \mathbf{u}_e^T \mathbf{k}_e^H(\hat{\mathbf{c}}_e, \hat{v}_e) \mathbf{u}_e. \quad (\text{B21})$$

For the low-diversity penalty function, the sensitivity can be derived using chain rule by taking the gradient of the log-determinant ([Boyd and Vandenberghe, 2004](#)), then the Gaussian kernel and Euclidean distance between the class design variables, $\mathbf{c}^{(m)}$.

Finally, for the derivations of the first stage of the shape matching problem (Eq. 14), in which the target properties for each unit cell are optimized, we refer the reader to our previous work ([Wang et al, 2020a](#)). For the second stage where the classes and their distributions are optimized to match the target properties (Eq. 15), we do not write out the sensitivities here; however, their derivations are straightforward to calculate by following the same steps above, substituting compliance for the mean squared error (MSE) between target and designed effective properties.